PHYSICAL REVIEW E **92**, 042405 (2015)

Calculating the role of composition in the anisotropy of solid-liquid interface energy using phase-field-crystal theory

Bernadine A. Jugdutt,[1] Nana Ofori-Opoku,[1,2,3,4] and Nikolas Provatas[1]
[1]*Department of Physics, Centre for the Physics of Materials, McGill University, Montreal, QC, Canada*
[2]*Department of Materials Science and Engineering, McGill University, Montreal, QC, Canada*
[3]*Northwestern-Argonne Institute of Science and Engineering, Northwestern University, Evanston, Illinois, USA*
[4]*Materials Science and Engineering Division, National Institute of Standards and Technology, Gaithersburg, Maryland, USA*
(Received 3 July 2015; published 21 October 2015)

This work uses Ginzburg-Landau theory derived from a recent structural phase-field-crystal model of binary alloys developed by the authors to study the roles of concentration, temperature, and pressure on the interfacial energy anisotropy of a solid-liquid front. It is found that the main contribution to the change in anisotropy with concentration arises from a change in preferred crystallographic orientation controlled by solute-dependent changes in the two-point density correlation function of a binary alloy, a mechanism that leads to such phenomena as solute-induced elastic strain and dislocation-assisted solute clustering. Our results are consistent with experimental observations in recent studies by Rappaz *et al.* [J. Fife, P. Di Napoli, and M. Rappaz, Metall. Mater. Trans. A **44**, 5522 (2013)]. This is the first PFC work, to our knowledge, to incorporate temperature, pressure, and density into the thermodynamic description of alloys.

DOI: 10.1103/PhysRevE.92.042405 PACS number(s): 68.08.De, 68.35.bd, 68.35.Md

I. INTRODUCTION

Dendritic growth has been the focus of both theoretical and experimental studies for some time. As the main kinetic growth mechanism in solidification, dendritic structure also sets the template for microstructure patterning in metals throughout their processing cycle. Dendrites have long been understood to emerge as a result of thermal or diffusive instabilities in the solid-liquid interface and subsequently grow in the orientation of lowest stiffness [1], which is a measure of local changes in the capillary length that in turn controls the local dendritic undercooling for solidification.

It was typically thought that dendrite orientation in alloys was restricted to the primary crystallographic directions of the alloying species in question; for alloys made up of solute components with different preferred directions, a discontinuous switch in orientation was expected as composition was varied. However, experimental studies [2–4] have shown that, in fact, there exists a class of materials for which a *continuous* variation in orientation can be observed, which may depend on alloy composition [3,5].

To date there has been, to our knowledge, no systematic fundamental study of the possible mechanism behind the continuous variation of dendrite orientation in alloy materials. Most studies using molecular dynamics (MD) models have examined pure substances [6–9], with a focus on fluctuations, though the application of molecular dynamics to alloys is possible assuming the availability of appropriate alloy potentials. Traditional phase-field models of alloys are not appropriate to examine anisotropy as their description of the interface is phenomenological, by construction. Indeed, phase-field models must incorporate information about surface energy and interface kinetics derived from microscopic-level theories or by making contact with sharp interface models of solidification that contain microscopic-level parameters [1,10–12].

Among other modern numerical modeling techniques, the phase-field-crystal (PFC) method in particular has proven effective at discerning physical behavior at atomic length scales and diffusive time scales [13–16]. Complex amplitude Ginzburg-Landau theories derived directly from PFC [or from classical density functional theories (c-DFT)] incorporate properties emanating from density wave fluctuations in the liquid. Specifically, the connection of such complex amplitude theories with a liquid phase correlation function can offer insight about the relation of interfacial energy anisotropy to microscopic properties of the solidifying liquid [8,9,17–19]. Moreover, since PFC theory is based on an atomic-scale order parameter, the resulting GL theory also incorporates fundamental crystallographic information about the solidifying crystal phase into calculation of the interface anisotropy parameter.

This work uses a recent *structural* PFC (XPFC) alloy model [20,21] to derive an effective Ginzburg-Landau (GL) theory to investigate the mechanism behind the changing anisotropy of the solid-liquid interface energy in alloys. In particular, we restrict ourselves to the study of a binary alloy and the effect of altering alloy composition on the interfacial anisotropy. The present work extends previous research using PFC-type models to calculate surface energy anisotropy in pure materials [8,22,23] to the case of alloys. Results are compared to the experiments of Rappaz *et al.* [5] on the Al-Zn system.

This study incorporates both concentration and average density changes in the determination of the equilibrium bulk states of the model and, as such, into the calculation of surface energy; past work on this type on alloys assumed an average density of $n_0 = 0$ [23]. This is done by deriving the pressure-density-temperature (P-n_o-σ) phase diagram of the alloy. This is the first study to incorporate pressure and density into the thermodynamic descriptions of PFC alloys.

In what follows we present the details of the XPFC alloy model II, as well as the derivation of a set of complex amplitude equations derived from model III. Section V outlines the construction of a pressure-density-temperature phase diagram for alloys and applies it to the XPFC alloy free energy. Section VI presents calculations of interfacial energy from the model, as well as the method of extracting interface anisotropy. Results are analyzed with a focus on how anisotropy changes with the concentration of the alloying element. The significance of our results are discussed and compared with experimental work in Sec. VII.

II. XPFC MODEL OF BINARY ALLOYS

This section reviews a PFC-type model used to study structural transformations [20,24], hereafter referred to as the *XPFC alloy model*. The XPFC model has been coarse grained into a complex amplitude Ginzburg-Landau (GL) theory [21,25] and will be the main tool used to study interface energy anisotropy. For brevity, XPFC and GL theories will only be reviewed here.

A. Free energy functional

The derivation of the binary XPFC alloy model is motivated from classical density-functional theory of binary mixtures. It begins by defining the spatial density fields ρ_A and ρ_B of the two component species, A and B. This functional is then transformed in terms of the dimensionless total density field n and a fractional concentration field c, defined by

$$\begin{aligned} \rho &= \rho_A + \rho_B \\ n &= \rho/\rho^0 - 1 \\ c &= \frac{\rho_B}{\rho_A + \rho_B} = \frac{\rho_B}{\rho}, \end{aligned} \tag{1}$$

where the total reference density is $\rho^0 = \rho_A^0 + \rho_B^0$. In terms of these fields the alloy free energy was shown to reduce to

$$\begin{aligned} &\frac{\Delta F}{k_B T \rho^0} \\ &= \int d\vec{r} \left\{ \frac{n^2}{2} - \eta \frac{n^3}{6} + \chi \frac{n^4}{12} + \omega(n+1)\Delta F_{\text{mix}}(c) \right. \\ &\quad \left. + \alpha |\nabla c|^2 - \frac{1}{2} n \int d\vec{r}' \big[X_1(c) C_2^{AA} + X_2(c) C_2^{BB} \big] n' \right\}, \end{aligned} \tag{2}$$

where

$$\Delta F_{\text{mix}}(c) = (1-c)\ln\left(\frac{1-c}{1-c_0}\right) + c \ln\left(\frac{c}{c_0}\right) \tag{3}$$

represents the entropic mixing of the two fields, k_B is the Boltzman constant, T is the temperature, and $c_0 = \rho_B^0/\rho^0$ is a reference concentration. The other parameters and functional forms appearing in Eq. (2) are described in the following.

The parameters η, χ, and ω, though formally equal to 1, will hereafter be treated as free parameters used to control the density dependence of the ideal free energy for values away from the reference density ρ^0, i.e., to match the bulk Landau free energy to material properties. This is loosely justified by noting that the $k = 0$ mode of higher-order correlation functions in c-DFT will contribute local polynomial terms in c and n of unknown magnitude [25]. It is thus practical to introduce the parameter set $\{\eta, \chi, \omega\}$.

The second line of Eq. (2) is the excess free energy. The first excess term accounts for fluctuations in concentration through the Cahn-Hilliard parameter α. Its value is related to the differences in particle correlation functions at $k = 0$ [20,26]. It is treated as a constant here since the objective is to study the role of such parameters on anisotropy.

The second excess term accounts for A-A interactions (C_2^{AA}), B-B interactions (C_2^{BB}), and A-B interactions through the concentration-dependent interpolation functions $X_1(c)$ and $X_2(c)$, which are discussed below. The core component of XPFC-type models is the single particle correlation function, the form of which is given in k space by Ref. [27],

$$\hat{C}_{2j}^{ii}(|\vec{k}|) = e^{\frac{-\sigma^2(|\vec{k}_j^i|)^2}{2\rho_j^i \beta_j^i}} e^{\frac{-(|\vec{k}| - |\vec{k}_j^i|)^2}{2(\alpha_j^i)^2}}, \tag{4}$$

where $\vec{k}_j^i$ is the reciprocal lattice vector defining the j^{th} mode or family of lattice planes in the crystal structure of element i. The constants ρ_j^i and β_j^i are constants representing the planar atomic density and the number of planar symmetries, respectively, of the j^{th} family of planes of element i. α_j^i is used to control the elastic modulus of element i in the direction of lattice planes j [28]. The model temperature is controlled by the parameter σ. The full correlation function of species i, denoted $\hat{C}_2^{ii}(|\vec{k}|)$, is the envelope of $\sum_j \hat{C}_{2j}^{ii}(\vec{k})$.

The competition in alloy systems between A-dominant and B-dominant crystal structures is predominantly modulated via changes in concentration c. This is effected through concentration-dependent correlations in the total density n. In theory, the density excess term in Eq. (2) will contain an infinite series of multipoint correlation functions of all orders, each multiplied by a polynomial (of the corresponding order) in c and $(1 - c)$. Since the form of these correlation functions is not known, we model the effect of concentration on two-point correlations in the total density through an effective two-point correlation function of the form

$$C_{\text{eff}}(|\vec{r} - \vec{r}'|) = \sum_{i=1}^{N} X_i(\{c_j\}) C_2^{ii}(|\vec{r} - \vec{r}'|), \tag{5}$$

where N is the number of solute species and $\{c_j\}$ represents the set of solute species in the alloy ($j = 1, \ldots, N$). In this study $N = 2$, $\{c_i\} = c$ and the $X_i(c)$ used are given by

$$\begin{aligned} \chi_1(c) &= 1 - 3c^2 + 2c^3 \\ \chi_2(c) &= 1 - 3(1-c)^2 + 2(1-c)^3. \end{aligned} \tag{6}$$

Equations (6) were derived in Ref. [24] and provide a robust way to model quantitatively the form of numerous experimentally relevant phase diagrams for practical alloys. In this study we will work with an alloy system similar to Al-Zn.

B. Euler-Lagrange equations

This section derives equations for the equilibrium solutions for the n and c fields in an XPFC binary alloy. Working in the grand-canonical ensemble, we begin by minimizing the grand potential functional given by

$$\Omega[\rho_A, \rho_B] = \tilde{F}[\rho_A, \rho_B] - \mu_A \int \rho_A(\vec{r}) d\vec{r} - \mu_B \int \rho_B(\vec{r}) d\vec{r}, \tag{7}$$

where $\tilde{F}$ represents the free-energy functional written in terms of the density fields ρ_A and ρ_B, while μ_A, μ_B are the chemical potentials of the respective species. Equilibrium fields are defined through the minimization of the grand potential,

$$\begin{aligned}\frac{\delta\tilde{F}[\rho_A,\rho_B]}{\delta\rho_A} &= \mu_A^{\text{eq}}\\ \frac{\delta\tilde{F}[\rho_A,\rho_B]}{\delta\rho_B} &= \mu_B^{\text{eq}}.\end{aligned} \tag{8}$$

In what follows, we will be using the variables n and c and as such need the corresponding Euler-Lagrange equations in these fields. Applying the variable transformation in Eq. (1) to Eq. (7) yields

$$\begin{aligned}\Omega[n,c] = F[n,c] - \mu_{\text{eq}}\int(n(\vec{r})+1)c(\vec{r})d\vec{r}\\ -\mu_A\int(n(\vec{r})+1)d\vec{r}.\end{aligned} \tag{9}$$

It is straightforward to show using the functional chain rule and Eq. (8) that the variational of $\delta\Omega[\rho_A,\rho_B]/\delta\rho_A = \delta\Omega[\rho_A,\rho_B]/\delta\rho_B = 0$ leads to $\delta\Omega[n,c]/\delta n = \delta\Omega[n,c]/\delta c = 0$. Thus, the Euler-Lagrange equations with respect to the fields c and n become

$$\begin{aligned}\frac{\delta F}{\delta n} &= \mu^{\text{eq}}c(\vec{r}) + \mu_A^{\text{eq}}\\ \frac{\delta F}{\delta c} &= \mu^{\text{eq}}[n(\vec{r})+1],\end{aligned} \tag{10}$$

where $F \equiv \Delta F/k_B T\rho^o$ and where we have defined a chemical interdiffusion potential as $\mu^{\text{eq}} \equiv \mu_B^{\text{eq}} - \mu_A^{\text{eq}}$.

It is noteworthy to consider the difference in conservation laws satisfied by (ρ_A,ρ_B) versus (n,c). In particular, since ρ_A and ρ_B represent physical density fields of each species, they satisfy

$$\begin{aligned}\int\rho_A(\vec{r})\,d\vec{r} &= \text{const}\\ \int\rho_B(\vec{r})\,d\vec{r} &= \text{const}.\end{aligned} \tag{11}$$

From the definition of $n = \rho_A + \rho_B$, it is clear that n is also a conserved field, i.e.,

$$\int n(\vec{r})\,d\vec{r} = \text{const}. \tag{12}$$

However, the field c is not generally globally conserved, as can be seen from its definition. This does not cause any problems when considering equilibrium properties of the model; care must be taken when describing dynamical evolution, however. One must formally begin form conservation equations for ρ_A and ρ_B and use the transformations in Eq. (1) to arrive at appropriate equations for n and c, which convolve both fields.

III. AMPLITUDE REPRESENTATION OF XPFC MODEL

The long-wavelength limit of Eqs. (10) is derived through a coarse-graining procedure applied to the original XPFC free energy. Equations generated from the coarse-grained free energy are known as *amplitude* equations. Their value is to make a connection with the length scales of traditional phase-field theories. Working with amplitude equations is also useful for practical reasons as it is nontrivial to numerically stabilize an equilibrium profiles of the microscopic XPFC model when variable average density and concentration are permitted.

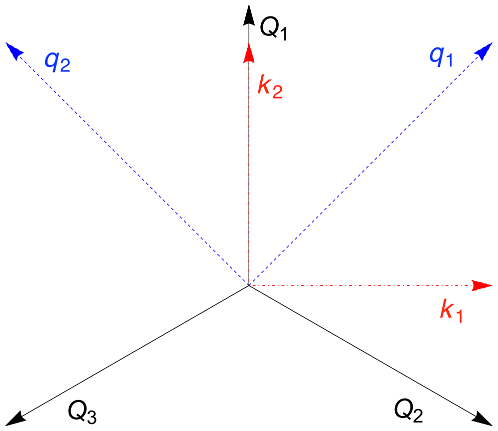

FIG. 1. (Color online) Reciprocal basis vectors to simultaneously represent square and triangular symmetries. Vectors $\vec{Q}_1$, $\vec{Q}_2$, and $\vec{Q}_3$ make up the single-mode triangular lattice description, while $\vec{k}_1,\vec{k}_2$ describe the first mode of the square and $\vec{q}_1,\vec{q}_2$ the second.

Coarse graining of the binary XPFC free energy is done via volume-averaging techniques developed in Refs. [21,25]. This method is based on a standard ansatz to break down the density field into a density wave decomposition that allows the representation of crystal symmetries available to the full XPFC model. Here we limit ourselves to the square-triangle phases of a eutectic binary alloy system. The total density expansion for the solid phase in this system is represented by

$$n(\vec{r}) = n_0 + \sum_{j=1}^{2}\mathcal{A}_j e^{i\vec{k}_j\cdot\vec{r}} + \sum_{l=1}^{2}\mathcal{B}_l e^{i\vec{q}_l\cdot\vec{r}} + \sum_{m=1}^{3}\mathcal{C}_m e^{i\vec{Q}_m\cdot\vec{r}}, \tag{13}$$

where $n_0(\vec{r})$ is the average density; $\mathcal{A}_j$ and $\mathcal{B}_l$ are the (in general complex) amplitudes controlling density variation in the (1,0) and (1,1) directions, respectively, of a square lattice; and $\mathcal{C}_m$ are the amplitudes controlling density variations in the three directions of a triangle phase. The reciprocal lattice vectors for each mode in Eq. (13) are shown in Fig. 1.

The density mode expansion in Eq. (13) is substituted into the binary XPFC free energy, after which a smoothing procedure is carried out whereby spatial oscillations on a scale several times greater than the lattice constant are integrated out. This yields a Ginzburg-Landau free energy F_{CG} that is a function of n_o, c, and $\{\mathcal{A}_j,\mathcal{B}_l,\mathcal{C}_m\}$. Since we wish here to examine only the influence of crystal structure and solute on the interface energy, we ignore the effects of elasticity and topological defects in solid phases. This amounts to assuming that the amplitudes of each mode of Eq. (13) are real. It is necessary to track $\{\mathcal{A}_j,\mathcal{B}_l,\mathcal{C}_m\}$ separately in order to retain an explicit angular dependence with respect to interface orientation.

The coarse-grained free energy $F_{\rm CG}[c,n_o,\mathcal{A}_j,\mathcal{B}_l,\mathcal{C}_m]$ for the XPFC alloy model is quite extensive and is thus reproduced in Eq. (A1). For details the reader is referred to Refs. [20,21,29]. In terms of $F_{\rm CG}$, the Euler-Lagrange equations for the $\{n_o,c,\mathcal{A}_j,\mathcal{B}_l,\mathcal{C}_m\}$ become

$$\begin{aligned}\frac{\delta F_{\rm CG}}{\delta n_o} &= \mu^{\rm eq} c(\vec{r}) + \mu_A\\ \frac{\delta F_{\rm CG}}{\delta c} &= \mu^{\rm eq}\{n_o(\vec{r})+1\}\\ \frac{\delta F_{\rm CG}}{\delta \mathcal{A}_j} &= 0\\ \frac{\delta F_{\rm CG}}{\delta \mathcal{B}_l} &= 0\\ \frac{\delta F_{\rm CG}}{\delta \mathcal{C}_m} &= 0.\end{aligned} \tag{14}$$

It is noted that the first two equations follow from Eq. (10), except they now involve the *average* density n_o and concentration c. These fields vary on the scale of the amplitudes in the density expansion in Eq. (13) [25]. The chemical potentials $\mu_A^{\rm eq}$ and $\mu^{\rm eq}$ are as in Eq. (10). The amplitudes are nonconserved parameters and thus simply minimized subject to all parameters and field configurations of n_o and c.

Equations (14) are solved in one dimension. The angle θ of the interface normal $\vec{n}$ with respect to a horizontal reference axis is taken into account by projecting the gradients in Eq. (A1) along $\hat{n}$, and writing $\vec{k}\cdot\nabla \rightarrow \vec{k}\cdot\hat{n}\,\partial_u$, where u is the direction transverse to the interface and $\vec{k}$ is a reciprocal lattice vector.

Equations (14) are subject to boundary conditions that define solid-liquid equilibrium. With respect to the normal coordinate u, these are given by

$$\begin{aligned}\lim_{u\rightarrow\pm\infty} n_o(u) &= n_{L,S}\\ \lim_{u\rightarrow\pm\infty} c(u) &= c_{L,S}\\ \lim_{u\rightarrow\pm\infty} \Phi_k(u) &= \Phi_k(c_{L,S},n_{L,S};\sigma,p),\end{aligned} \tag{15}$$

where $n_{L,S}$ and $c_{L,S}$ describe the liquid (L) and solid (S) values of the average density and concentration, while Φ_k stands for one of $\{\mathcal{A}_j,\mathcal{B}_l,\mathcal{C}_m\}$. The procedure for determining $\{c_S,c_L,n_S,n_L,\mu^{\rm eq},\mu_A\}$ is deferred to Sec. V.

IV. NUMERICAL SOLUTION OF EULER-LAGRANGE EQUATIONS

The Euler-Lagrange equations in Eq. (14) are solved in one dimension at constant model temperature (σ) and pressure (p) using a simple pseudotime algorithm given by

$$n_0{}^{t+1} = n_0{}^{t} + dt\,M\left(\mu_{\rm eq}c + \mu_a - \frac{\delta F_{\rm CG}}{\delta n_0}\right), \tag{16}$$

$$c^{t+1} = c^{t} + dt\,M\left[\mu_{\rm eq}(n_0+1) - \frac{\delta F_{\rm CG}}{\delta c}\right], \tag{17}$$

for n_o and c, and

$$\begin{aligned}\mathcal{A}_j{}^{t+1} &= \mathcal{A}_j{}^{t} - dt\,M\frac{\delta F_{\rm CG}}{\delta \mathcal{A}_j}\\ \mathcal{B}_l{}^{t+1} &= \mathcal{B}_l{}^{t} - dt\,M\frac{\delta F_{\rm CG}}{\delta \mathcal{B}_l}\\ \mathcal{C}_m{}^{t+1} &= \mathcal{C}_m{}^{t} - dt\,M\frac{\delta F_{\rm CG}}{\delta \mathcal{C}_m}\end{aligned} \tag{18}$$

for the amplitude equations, where j, l, and m run over the indices associated with each amplitude in the density expansion sum of Eq. (13) and where M is constant to affect convergence time. The results of this work are independent of M. At each time step, far-field boundary conditions determined from Eq. (15) are applied.

It is noted that while Eqs. (16)–(18) are numerically practical to implement, it was found that the driving forces never become exactly zero. As such the interface drifts a little as the system starts to melt, as Eqs. (16) and (17) are not conserved equations. This numerical artifact has also been seen in past simulations done with $n_0 = 0$ [17], but was small enough that the evolution of the system was unaffected over the time scale of convergence of the excess free energy characterizing the solid-liquid energy. This issue is alleviated by decreasing the spacial and pseudo time steps (dx and dt, respectively), but this is impractical due to the drastic increase simulation time. Instead, it is emphasized that the interface structure and interface energy both converge to their final values very rapidly, in all cases before any appreciable interface translation toward complete melting occurs; the time scales for the system to melt entirely are approximately an order of magnitude longer than those for the grand potential of the system to converge, as shown in Fig. 2. Since this translation *does not* involve *any* shifting of far-field bulk values of the fields, the excess free energy in all results reported here converges well before this numerical artifact becomes observable. We take our system to be converged when the total grand potential of the system has stopped changing up to 10^{-9}.

An alternate, more precise, numerical method to eliminate the drifting is to replace the first of Eq. (18) by

$$n_0^{t+1} = n_0^{t} + dt M\nabla^2\left(\frac{\delta F_{\rm CG}}{\delta n_0} - \mu_{\rm eq}c\right) \tag{19}$$

and apply periodic boundary conditions. This is essentially a conservation equation that adjusts the drifting of the fields such that μ_A is "pinned" to a constant consistent with the equilibrium $\mu_{\rm eq}$, which is a function of the pressure. We have confirmed that both methods reproduce the same results for the surface energy.

V. PHASE COEXISTENCE IN PRESSURE-TEMPERATURE-CONCENTRATION-DENSITY SPACE

A major result of this work is the construction of a three-dimensional density (n_o)–concentration (c)–temperature (σ) phase diagram of an XPFC alloy. This is significant as past work with alloy PFC models has been limited to constructing a two-dimensional (2D) phase diagram in concentration and temperature, around a density $n_o = 0$. This simplification,

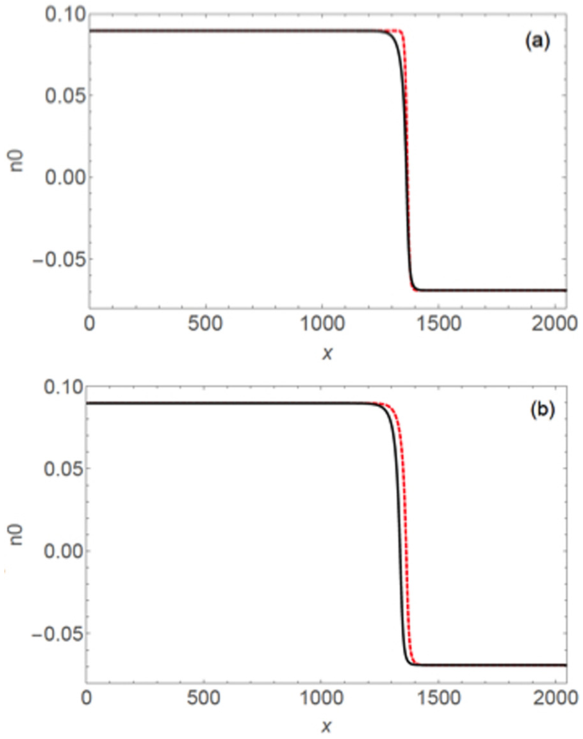

FIG. 2. (Color online) Sample one-dimensional density profiles from our simulations to illustrate convergence of their form. (a) The dashed red line is the interface at $t = 0$; solid black line is the equilibrium interface converged at $t = 6515$. (b) The dashed red line is the converged $t = 6515$ profile; the solid black line is the interface at $t = 60\,000$. While the profile has been slightly translated to the left, its shape rapidly converges as does the excess free energy computed form it.

however, does not maintain a constant pressure for all points on the 2D concentration-temperature phase diagram.

A. Coexistence conditions

To construct a numerical phase diagram, we neglect spatial gradients in $F_{\rm CG}$ [Eq. (A1)] and retain the minimal number of modes stabilizing the crystal structure of a desired solid phase. Furthermore, for the purposes of constructing a phase diagram we do not require an explicit angular dependence and as such we can assign all members of an amplitude set to the same value, that is, $\mathcal{A}_j = \mathcal{A}$, $\mathcal{B}_l = \mathcal{B}$, and $\mathcal{C}_m = \mathcal{C}$. A single mode is required for the triangle phase ($\mathcal{A} = \mathcal{B} = 0$) in Eq. (13), yielding

$$\begin{aligned} F_{\rm tri}(n_o,c) = {} & 3\big(1 - n_0\eta + n_0^2\chi\big)\mathcal{C}^2 + 2(2n_0\chi - \eta)\mathcal{C}^3 \\ & + 15\frac{\chi}{2}\mathcal{C}^4 + \frac{n_0^2}{2} - \eta\frac{n_0^3}{6} \\ & + \chi\frac{n_0^4}{12} - 3\hat{C}_{\rm eff}\big(\big|\vec{k}_{10}^B\big|\big)\mathcal{C}^2, \end{aligned} \tag{20}$$

where $\vec{k}_{10}^B$ denotes a reciprocal lattice vector that sets the length scale for a triangular lattice favoured by element B in this work. For the square phase, a two-mode approximation is required [$\mathcal{C} = 0$ in Eq. (13)], yielding

$$\begin{aligned} F_{\rm sq}(n_o,c) = {} & 2\big(1 - n_0\eta + n_0^2\chi\big)(\mathcal{A}^2 + \mathcal{B}^2) + 3\chi^2(\mathcal{A}^4 + \mathcal{B}^4) \\ & + 4(2n_0\chi - \eta)\mathcal{A}^2\mathcal{B} + 12\chi\mathcal{A}^2\mathcal{B}^2 \\ & + \frac{n_0^2}{2} - \eta\frac{n_0^3}{6} + \chi\frac{n_0^4}{12} \\ & - 2\hat{C}_{\rm eff}\big(\big|\vec{k}_{10}^A\big|\big)\mathcal{A}^2 - 2\hat{C}_{\rm eff}\big(\big|\vec{k}_{11}^A\big|\big)\mathcal{B}^2, \end{aligned} \tag{21}$$

where $\vec{k}_{10}^A$ and $\vec{k}_{11}^A$ are the first and second reciprocal lattice vectors of the square phase, which set the two length scales for the preferred crystal lattice of element A. Finally, in the above,

$$\hat{C}_{\rm eff}(|\vec{k}|) = \sum_{i=1}^{2} X_i(c)\hat{C}_2^{ii}(|\vec{k}|) \tag{22}$$

is the effective correlation function in k space [see Eq. (5)].

Equations (20) and (21) are numerically minimized with respect to $\mathcal{C}$ and $\{\mathcal{A},\mathcal{B}\}$, respectively. The solutions are substituted back into Eqs. (20) and (21), yielding lengthy expressions for the solid free energies that are evaluated numerically [29]. Furthermore, setting all amplitudes to zero yields the reference liquid free energy, denoted hereafter $F_L(n_o,c)$.

To calculate the required equilibrium (far-field) values in density and concentration for coexisting solid and liquid phases, four independent equations must be solved. First is the equality of chemical potentials μ_A and $\mu_{\rm eq} = \mu_B - \mu_A$ in each phase. This gives

$$\mu_{\rm eq} = \frac{1}{n_S + 1}\frac{\partial F_S}{\partial c_S} = \frac{1}{n_L + 1}\frac{\partial F_L}{\partial c_L}, \tag{23}$$

$$\mu_A = \frac{\partial F_S}{\partial n_S} - \frac{c_S}{n_S + 1}\frac{\partial F_S}{\partial c_S} = \frac{\partial F_L}{\partial n_L} - \frac{c_S}{n_L + 1}\frac{\partial F_L}{\partial c_L}, \tag{24}$$

where F_S is either of $F_{\rm tri}$ or $F_{\rm sq}$. In addition, the pressure in solid and liquid must be the same. Pressure is given by $p = -\Omega$, implying

$$p = (n_S + 1)\frac{\partial F_S}{\partial n_S} - F_S = (n_L + 1)\frac{\partial F_L}{\partial n_L} - F_L. \tag{25}$$

By fixing the temperature σ *and* the pressure p of the system, Eqs. (23)–(25) yield the following set of four equations:

$$\mu_{\rm eq}^L(\sigma,n_L,c_L) = \mu_{\rm eq}^S(\sigma,n_S,c_S), \tag{26}$$

$$\mu_A^L(\sigma,n_L,c_L) = \mu_A^S(\sigma,n_S,c_S), \tag{27}$$

$$p^L(\sigma,n_L,c_L) = p, \tag{28}$$

$$p^S(\sigma,n_S,c_S) = p, \tag{29}$$

where $\mu_{\rm eq}^S/\mu_A^S/p^S$ and $\mu_{\rm eq}^L/\mu_A^L/p^L$ are shorthand for the middle and right-hand expressions, respectively, in Eqs. (23)–(25). These equations are solved to obtain equilibrium values for n_S,n_L,c_S,c_L. We can additionally calculate numerical values of the mode amplitudes from these far-field values. Once solved, the left-hand sides of Eqs. (23)–(24) also yield $\mu_{\rm eq}$ and μ_A, respectively.

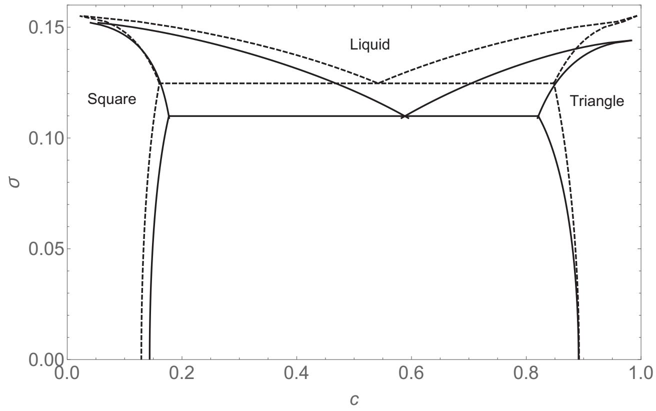

FIG. 3. Binary alloy phase diagram; the solid line is calculated with $n_0 = 0$ while the dashed line is a c-σ projection of a c-n_0-σ phase diagram at a constant pressure of $p = -0.07$. The eutectic point shifts from a model temperature of $\sigma = 0.10$ for the $n_0 = 0$ case to $\sigma = 0.125$ for the constant pressure case.

It is important to note that not every combination of average values n_0, c_0 leads to coexistence at any given pressure; herein lies a problem with the $n_0 = 0$ simplification, which assumes that all of the concentration space can be accessed at a constant average density. Indeed, in order for this to be true, pressure must be varied. From the full set of far-field values that emerge from Eqs. (26)–(29), we must equate the density and concentration lever rules, i.e.,

$$\frac{c_0 - c_L}{c_S - c_L} = \frac{n_0 - n_L}{n_S - n_L}, \tag{30}$$

to solve for the allowable range of n_0 and c_0 (or vice versa), for given temperature *and* pressure parameters.

B. Numerical phase diagrams

We present the numerically calculated phase diagrams for a eutectic binary alloy with square and triangular solid phases and having equal first correlation peak width in both species, that is, $\alpha_{10}^A = \alpha_{10}^B = 1.5$. The stiffness parameter for the second length scale of the square is chosen as $\alpha_{11}^A = \sqrt{2}\alpha_{10}^A$ in order to preserve elastic isotropy in the square phase [24].

By way of analogy with the simplified $n_0 = 0$ phase diagram construction, Fig. 3 presents a constant pressure alloy phase diagram in variables c and σ, which comes from a constant-pressure phase diagram in the variables c, n_0, and σ projected onto the temperature-concentration axes. We see the same general shape in the phase diagram, but notably the eutectic has shifted away from the $n_0 = 0$ approximation.

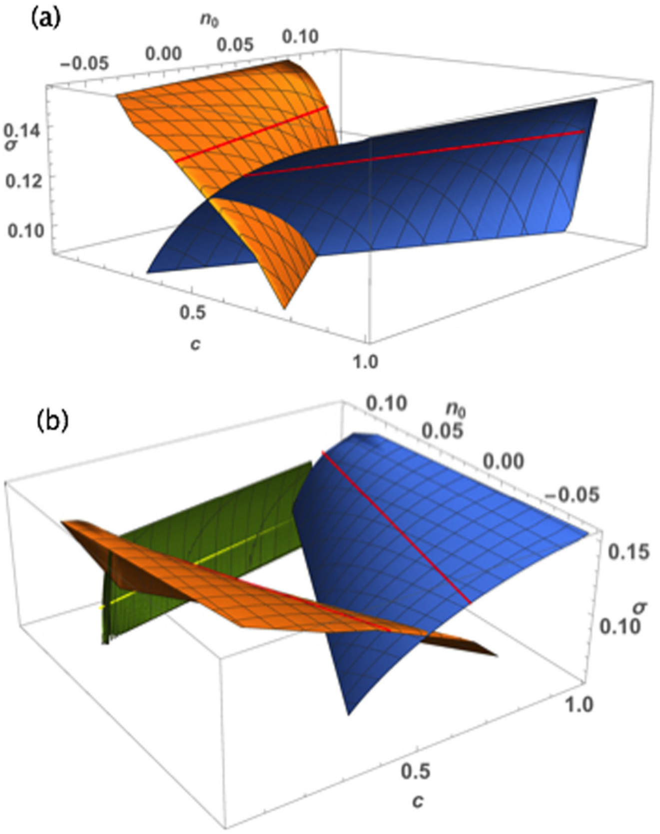

FIG. 4. (Color online) (a) Solid-liquid coexistence regions of the binary alloy phase diagram in 3D temperature (σ), concentration (c_0), and density (n_0) space at a constant model pressure, $p = -0.07$. The orange (lighter surface to the left) represents the square-liquid coexistence plane, while the blue (darker surface to the right) is the triangle-liquid. The solid red line across each plane indicates coexistence tie lines. The line defined by intersecting surfaces is the eutectic line; note the change of eutectic temperature as a function of n_o. (b) Rotated view of above (square-liquid on the left; triangle-liquid on the right), but including in green solid-solid coexistence region (flattened surface at rear of the figure with tie line in yellow); note the limited region of density space where such coexistence is possible.

Figure 4 shows a 3D c, n_0, and σ phase diagram at constant model pressure of $p = -0.07$. The planar surfaces in the topmost image represent the solid-liquid coexistence regions for the square [orange (lighter surface)] and triangle [blue (darker surface)] phases. The area above the curves corresponds to the liquid region of the phase diagram and below to the solid region. The negative-most and positive-most edges of these surfaces along n_o are the respective solidus and liquidus lines, while points anywhere along the red lines traversing each surface represent average values c_0, n_0, that can yield coexisting solid-liquid phases at a fixed temperature and pressure. The line at which the two surfaces intersect defines a eutectic line in (c,n_o,σ) space. The flatter green surface in the bottom image represents the solid-solid coexistence region, which exists only for a limited range of densities n_0, in contrast to the solid-liquid regions.

C. Pressure space projection of numerical phase diagram

It is also possible to construct a constant-temperature phase diagram displaying the pressure-concentration equilibrium of the alloy. Figure 5 shows the pressure-concentration phase diagram for a binary alloy at a constant model temperature $\sigma = 0.12$. At constant σ and decreasing p the phase diagram mimics the behavior seen for constant p and increasing σ. Note in particular that the respective sizes of the square and triangle solid-liquid coexistence regions are comparable to those seen

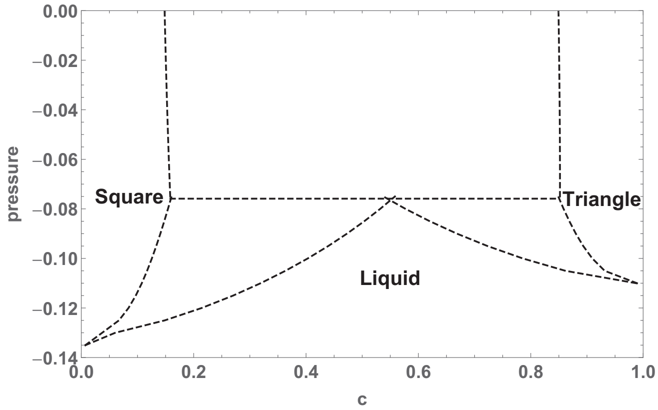

FIG. 5. c-p phase diagram for a binary alloy projected from a three-dimensional c-p-n_0 phase diagram for the case of constant model temperature $\sigma = 0.12$. The shape is an inversion of the typical temperature-concentration phase diagram, with a "eutectic pressure" at $p = -0.75$.

in Fig. 3. We also note the presence in this case of a "eutectic pressure" for the constant temperature case, located at roughly $p = -0.75$.

Figure 6 presents pressure-concentration cuts of the triangle-liquid coexistence region in Fig. 5 at different σ. This clearly shows the manner in which both the shape and position of the major features of the liquidus and solidus lines vary with temperature.

The pressure dependence of the binary alloy phase diagram is clearly significant and may strongly impact the potential of a simulation to stabilize certain structures and/or coexistence regions. Care must therefore be taken, especially when comparing PFC simulations to experimental work, to ensure that simulations conform to a constant pressure. The results of this section will be used in what follows to perform constant pressure simulations to investigate the solid-liquid interface of a binary alloy derived from the XPFC model.

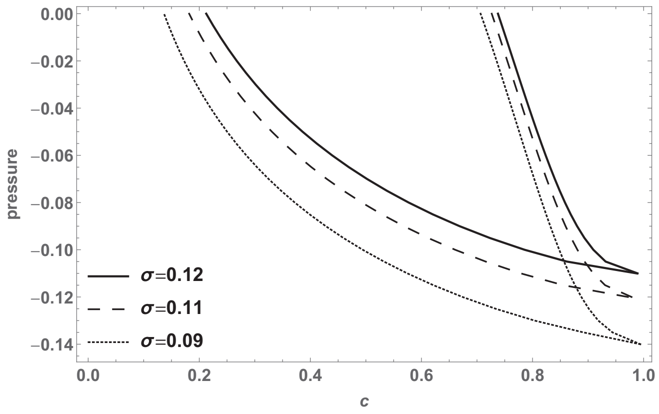

FIG. 6. Pressure-concentration curves plotted for three temperatures for the triangle-liquid coexistence region of the phase diagram in Fig. 5. Both the position and the width of the coexistence region changes with temperature.

VI. CALCULATING INTERFACIAL ENERGY

The interfacial energy is measured via the alloy grand potential

$$\Omega[c,n_o] = F_{\mathrm{CG}}[c,n_o] - \mu_A \int d\vec{r}(n_o+1) - \mu_{\mathrm{eq}} \int d\vec{r}\, c\,(n_o+1) \tag{31}$$

written in terms of the coarse-grained free energy F_{CG} and the smoothed fields n_o and c. Subtracting the bulk grand potential (calculated from either the solid or liquid region) from the total,

$$\Omega_{\mathrm{interface}} = \Omega_{\mathrm{total}} - \Omega_{\mathrm{bulk}}, \tag{32}$$

defines the excess free energy of the solid-liquid interface. To calculate the unit interfacial energy, γ_{sl}, we divide by the interface length, obtaining

$$\begin{aligned}\gamma_{\mathrm{sl}} &= \frac{\Omega_{\mathrm{total}} - \Omega_{\mathrm{bulk}}}{L_{\mathrm{int}}}\\ &= \frac{1}{L_{\mathrm{int}}}\bigg(\int d\vec{r}\{(F_{\mathrm{CG}} - F_{S/L}) + \mu_A(n_{S/L} - n_o)\\ &\quad + \mu_{\mathrm{eq}}[c_{S/L}\,(n_{S/L}+1) - c\,(n_o+1)]\}\bigg),\end{aligned} \tag{33}$$

where $F_{S/L}$ is the coarse-grained bulk free energies, $c_{S/L}$ is the far-field concentrations, and $n_{S/L}$ is the far-field average densities in the bulk solid and liquid phases, respectively. Equation (33) will be used in the next section to compute the surface energy and its anisotropy in binary alloys.

A. Fitting the anisotropy

Consider the equation used to fit the interfacial energy data from our simulations

$$\gamma_{sl}(\theta) = \gamma_0\,(1 + \epsilon_4 \cos 4\theta + \epsilon_8 \cos 8\theta + \cdots). \tag{34}$$

In fitting simulation data for $\gamma_{\mathrm{sl}}(\theta)$, Eq. (34) can be taken to any desired order, where contributions from successive orders yield smaller and smaller corrections to γ_{sl}. We desire the smallest order expansion that accurately captures the behavior of the stiffness $S(\theta) = \gamma_{\mathrm{sl}}(\theta) + \gamma_{\mathrm{sl}}''(\theta)$, where primes denote differentiation with respect to θ. Past work with pure materials and alloys of species with symmetric phase diagrams found a first-order fit to be sufficient. However, in those situations both species (for the case of alloys) had the same preferred crystal structure and as such no competition between crystal structures was seen; in such a situation it is reasonable to expect a simple first-order fit to be sufficient to capture the stiffness.

In this work the presence of a species minimized by a triangle crystal structure but existing in a square phase has a pronounced effect on the interfacial energy; a first-order expansion results in a notably poor fit to the data. We must be careful, however, in considering higher-order terms, as anisotropies in γ_{sl} are exaggerated in the stiffness S, and care must be taken that artificial angular dependencies introduced by higher-order fits to $\gamma_{\mathrm{sl}}(\theta)$ are eliminated by systematically determining a fitting order beyond which spurious angular dependencies stop occurring. We find in particular that a second-order fit introduces an artificial local maximum in stiffness at the location of the global minimum for higher-order fits; to avoid such misleading results we studied taking successively higher-order fits until no significant change occurred in the resulting stiffness curves. We found that this can be ensured by using a sixth-order fit to $\gamma_{\rm sl}$,

$$\gamma_{\rm sl} = \gamma_o(1 + \epsilon_4 \cos 4\theta + \epsilon_8 \cos 8\theta + \epsilon_{12} \cos 12\theta + \epsilon_{16} \cos 16\theta + \epsilon_{20} \cos 20\theta + \epsilon_{24} \cos 24\theta). \quad (35)$$

It is noted that some important features of the stiffness anisotropy curve can still be well reproduced by the first-order fit, specifically, the number of minima and maxima and their position in terms of angle. The values of the lowest-order fitting parameters γ_0 and ϵ_4 only change by 0.002% and 0.2%, respectively, from a first-order to a sixth-order fit. For regions where a double local minima may exist in stiffness (not seen in our work but observed by Gonzales and Rappaz [5] for a composition of 0.58), the third-order fit should be adequate to maintain an accurate global minimum while also sustaining the presence of multiple local wells or peaks. In all cases a higher-order fit is required if information about the depth and steepness of the maxima or minima is desired. The stiffness and interfacial energy curves shown in the following sections were generated with a sixth-order fit; however, for the purposes of determining the direction of dendrite orientation we report only γ_o and ϵ_4. For details on the full range of fitting parameters in the data below, the reader is referred to Ref. [29].

B. Solute dependence of anisotropy

A continuous transition of surface anisotropy minima was reported experimentally in Al-Zn, as the concentration of Zn crosses over from the Zn-poor to the Zn-rich part of the phase diagram [5]. To investigate the mechanism of this continuous transition, we used the amplitude model derived in Sec. III to investigate a binary alloy with phase diagram shown in Fig. 7, which has similar features to that of Al-Zn. The XPFC alloy system is modelled by defining component A (which favors a square lattice) with a significantly higher stiffness than component B (which is set to favor a triangular lattice). The specific choice of parameters is listed in Table I. To obtain surface energy curves we initialized simulation profiles with far-field values for concentration and density obtained from the calculated phase diagram in Fig. 7; all simulations were performed at a constant pressure of $p = -0.07$. Simulations were considered equilibrated when the total grand potential value Ω converged with an error less than 10^{-9}. The resulting plots of surface energy $\gamma_{\rm sl}$ versus angle θ were fit to the form in Eq. (35), and stiffness plots obtained via $S = \gamma_{\rm sl} + \gamma_{\rm sl}''$.

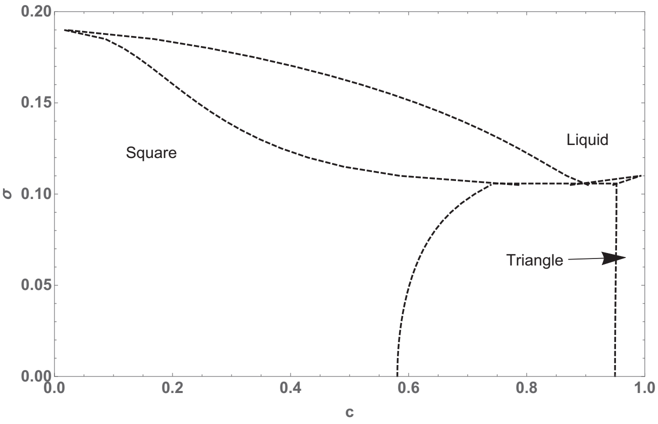

FIG. 7. Theoretical phase diagram obtained from the choice of XPFC parameters in Table I, in which the left-side (square) species strongly dominates. This was constructed at a constant model pressure of $p = -0.07$. This system has similarities with Al Zn.

TABLE I. Correlation function peak positions, widths, and heights ($\vec{k}^i_j$, α^i_j, and σ_M, respectively) used to create the square-biased binary alloy phase diagram.

$\vec{k}^i_j$	α^i_j	σ_M
$\vec{k}^A_{10}$	1	$\frac{\pi^2}{3}$
$\vec{k}^A_{11}$	$\sqrt{2}$	$\frac{2\pi^2}{3}$
$\vec{k}^B_{10}$	3.5	$\frac{8\pi^2}{9}$

We first consider the solid-liquid interface in the square-liquid coexistence region at a constant temperature σ and different values of average concentration c_0. In the context of a binary alloy, keeping the temperature constant amounts to staying on the same phase coexistence tie line and thus keeping the same far-field values for concentration and density. As a result, we do not expect to see a difference in the resulting interfacial profiles or excess energies. Simulation results confirm that there is no significant change in the resulting interfacial energy and stiffness curves.

We next scan the above system over temperature; each gives a different set of far-field values for the bulk fields. We see a clear change in the magnitude of interfacial energy and stiffness curves with temperature. This is shown in Fig. 8.

Before proceeding with the "model Al Zn" system in Fig. 7, it is pertinent to carefully consider what is being measured both in our simulations and in the experiments of Refs. [3,5], which observed a concentration-dependent change in dendrite orientation, providing strong motivation for this study. A change in stiffness anisotropy was observed with changing percentages of zinc via determination of the dendrite orientation of a fully solidified sample. Samples were solidified gradually via directional solidification, and results were presented both in terms of average composition and of nominal composition of the solid phase. For a sufficiently steady cooling rate the far-field solid composition will correspond to the solid composition from the last solid-liquid tie line encountered as the sample cools. In our simulations, each model temperature is thus associated with a particular tie-line composition of solid. This implies that the anisotropy behavior that we observe is the result of composition changes in the solid or at least a convolution of both concentration and temperature.

We next examine results for the Al Zn-like system obtained from the parameters in Table I. Figures 9 and 10 show the parameters γ_o and ϵ_4 resulting from fits to Eq. (35) in terms of both solidus concentration and temperature. Higher-order fitting parameters are omitted, but were found to follow the

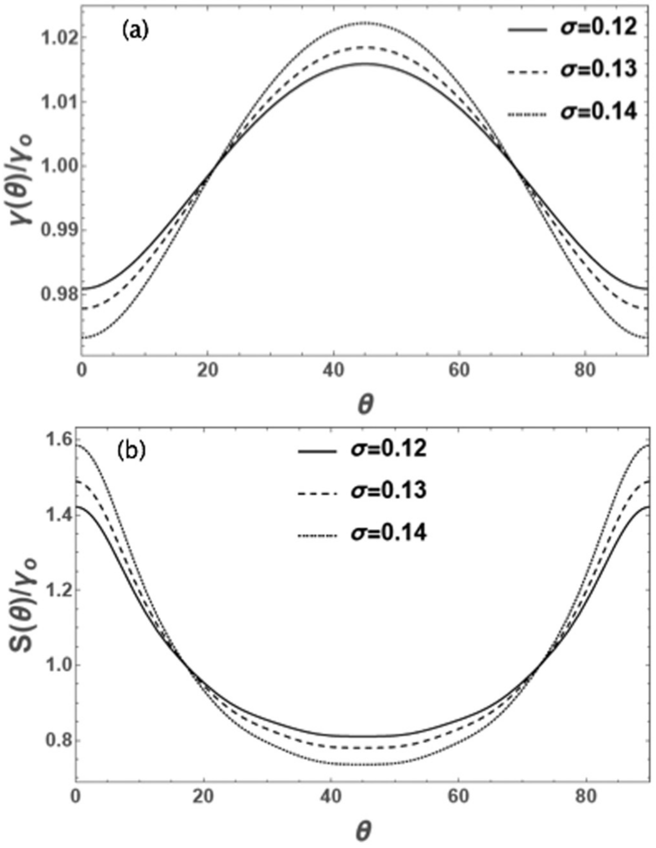

FIG. 8. (a) Interfacial energy γ and (b) stiffness S curves (normalized by the isotropic surface energy γ_o) for the $\alpha_{10}^A = \alpha_{10}^B = 1.5$ alloy system of Sec. V, shown for a constant average concentration $c_0 = 0.2$ and three model temperatures. The overall shape of the curves shown stays the same; however, there is a change in the heights of the respective maxima and minima.

same general trend as ϵ_4 and are of successively decreasing orders of magnitude (10^{-4} and smaller).

For high temperatures [low concentrations (c) of component B] the isotropic interface energy γ_o in Fig. 9 shows an increasing trend with decreasing temperatures (or with increasing c). This is analogous to the findings of other works that studied the role of interface energy in a isotropic Zn-Al system, over a limited range of Al concentrations and temperatures [17]. On the other hand, γ_o exhibits a maximum as temperature is further decreased or c is further increased.

The anisotropy parameter ϵ_4 in Fig. 10 exhibits a change of ~10% change over the range of concentrations (or temperatures) examined, significantly greater than the changes of 1% previously reported for a pure material [23]. This change of ~10% corresponds to change in solidus concentration on the order of 0.01. This change is on the same order of that reported by Gonzales and Rappaz [5] in experimental work over the same difference in solidus concentration.

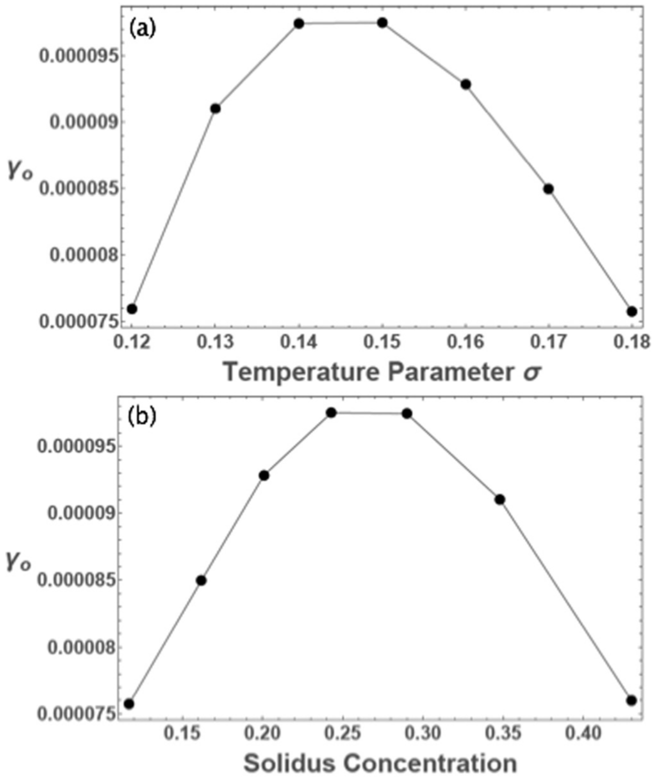

FIG. 9. The isotropic interface energy γ_o, plotted in terms of both (a) temperature and (b) associated solidus concentration.

It is plausible that the situation described by the data of Figs. 9 and 10 is explained by two competing effects not present in previous studies. At low concentration, the expected temperature dependence of the isotropy dominates. However, as concentration increases, increased amounts of the triangular-forming species (B) intrude on the dominant square phase. This will inhibit the formation of the species-A preferred square structure and cause the value of γ_o to tend toward a lower value consistent with presence of the lower-stiffness phase favored by the B atoms. Similarly, the anisotropy parameter of the solvent, which is more sensitive to temperature decreases than γ_o, begins to increase more slowly as c increases. In cases where the species A and B are of comparable stiffness, this effect is likely less pronounced and we expect the temperature dependence of these quantities to behave monotonically, at least for an extended range from that in Fig. 10. It is noteworthy that changes in γ_o are on the order of 10^{-5} (effectively constant on the scale of the anisotropy changes) and as such may not be large enough to be considered as important as the changes in the anisotropy parameter.

Figure 11 and Fig. 12 show, respectively, the interfacial energy curves γ/γ_o and normalized stiffness curves S/γ_o for different solidus concentrations. It is noted that as a solidus composition of 0.5 is approached, the global stiffness minimum at $\theta = 45°$ becomes much less well defined. In fact, for the highest concentrations, we see a range from roughly 30° to 60° where the stiffness curve is almost flat, suggesting there is no strongly preferred dendrite orientation within this range. These results agree well with behavior seen by Rappaz *et al.* at concentrations around 0.58. We have not been able to observe the flip of maxima to minima seen experimentally at high zinc concentrations. It is plausible that this is due the fact that we have not been able to accurately reproduce the long, thin isomorphous region of square-liquid coexistence in

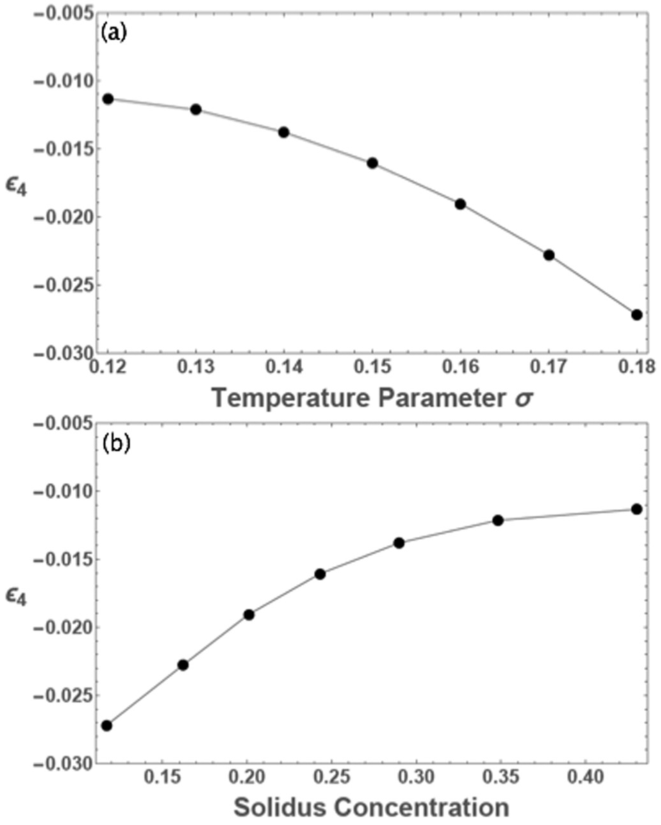

FIG. 10. The first-order anisotropic parameter ϵ_4 plotted in terms of both (a) temperature and (b) solidus concentration. In both plots ϵ_4 exhibits a plateau; it does so slightly more sharply in terms of concentration as sufficiently high concentration of the secondary species (B) is reached. Higher values of concentration were not attainable within the square solid-liquid coexistence region of this XPFC alloy system.

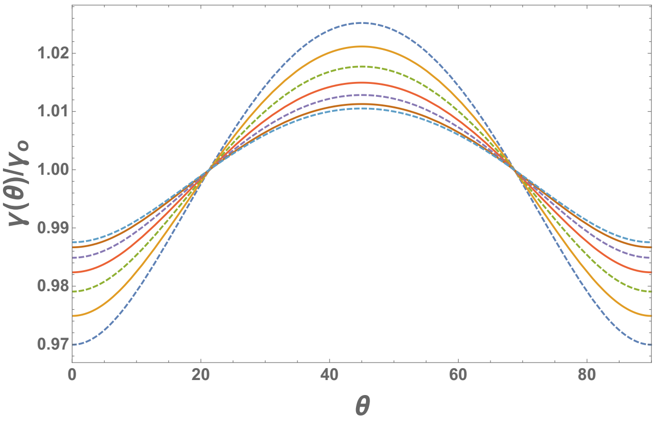

FIG. 11. (Color online) Normalized interfacial energies $\gamma(\theta)$ for the case of a large stiffness disparity between alloy species (alloy system of Fig. 7). The highest amplitude curves correspond to lowest solidus concentrations and vice versa. Concentrations shown are 0.117,0.162,0.201,0.243,0.290,0.348,0.430. These curves were used to extract the data in Figs. 9 and 10.

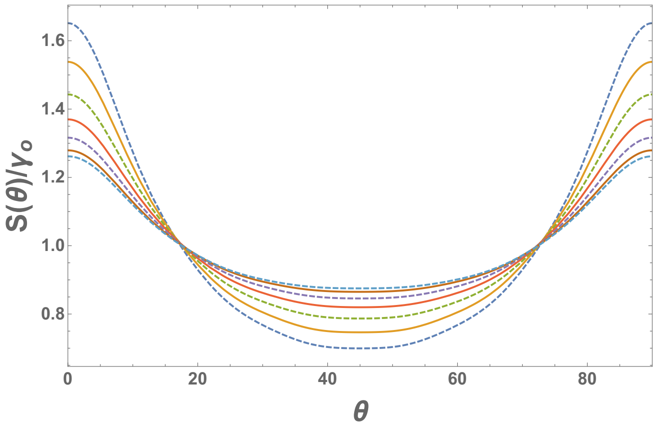

FIG. 12. (Color online) Normalized stiffness curves $S(\theta)/\gamma_o$ corresponding to the interfacial energy curves of Fig. 11. The highest amplitude curves correspond to lowest solidus concentrations and vice versa. Concentrations shown are 0.117,0.162,0.201,0.243,0.290,0.348,0.430.

our alloy system, analogously to the experimental Al-Zn phase diagram. Because of this we were not able to access such high solidus concentrations in our simulations.

VII. CONCLUSIONS

We derived a new Ginzburg-Landau theory based on a recent structural PFC model of binary alloys. We additionally derived a formalism for studying phase coexistence in our model in pressure-concentration-density-temperature space. The model was used to conduct constant pressure simulations to investigate the effect of solute species concentration, and temperature, on the solid-liquid interface energy and its anisotropy. Our model predicts a concentration dependence in the interface stiffness that originates in the elemental interactions inherited from the liquid state correlation functions built into the original XPFC theory.

Recent work by Rappaz and coworkers has reported a continuous transition in the anisotropy of the solid-liquid interface as the concentration of Zn is increased in Al-Zn alloys. Our simulations are consistent with these observations and suggest that the results are a consequence of solute (B) atoms infiltrating the preferred lattice structure of the solvent (A) species. Specifically, in the case where the two species prefer different lattice symmetries, and one of the species is sufficiently stiff in comparison to the other, we may not see a discontinuous transition from one preferred dendrite orientation to the other. Rather, the stiffer material holds on to its preferred structure while becoming “weaker” in the low stiffness direction corresponding to the second, softer, element. This can lead to flattened regions of the stiffness curve with no strongly preferred direction for dendrite growth.

We observed that the role of concentration, modulated by temperature, causes a much more significant change in interface anisotropy than is observed due to a change in temperature alone in a single component material.

We are unable in our simulation to completely separate the temperature and concentration dependence of the interfacial anisotropy, although a comparison of our constant-σ versus changing-σ anisotropy results does strongly suggest that the role of concentration on interface anisotropy is modulated by the temperature as a control. It is plausible that this convolved effect is a limitation of the accessible phase space of a binary alloy. A possible future direction for research is to move to a higher-order (i.e., ternary) alloy, thereby adding a second concentration field; this should create a phase space wherein multiple tie lines can be constructed for a fixed temperature. The presence of a coexistence plane rather than a coexistence line may be the key to deconvolve the effects of temperature and concentration in their role on interface energy.

ACKNOWLEDGMENTS

The authors thank The National Sciences and Engineering Research Council of Canada and the Canadian Research Chairs program for funding and Compute Canada for high performance computing resources.

APPENDIX: AMPLITUDE EXPANSION FREE ENERGY

The procedure for coarse graining the XPFC free energy in Eq. (2) uses a box or volume averaging method to project out the short-wavelength behavior of $n(x)$ onto the density amplitudes $\{\mathcal{A}_j,\mathcal{B}_l,\mathcal{C}_m\}$, the concentration c, and average density n_o. The procedure is too lengthy to review here but is thoroughly documented in Refs. [21,25,29]. For the alloy system, we employ a two-peaked correlation function that interpolates between square and triangular phases in 2D (FCC and BCC in 3D). A multimode expansion for $n(\vec{x})$ that allows for both these phases is given by Eq. (13). Since in this work elastic and plastic effects on the interface energy are neglected, the amplitude of each density wave is assumed to be real. In Eq. (13) there are two square modes (one with the two amplitudes $\mathcal{A}_j$ and the other with the two amplitudes $\mathcal{B}_l$) and one triangular mode with three amplitudes $\mathcal{C}_m$. Under these conditions, coarse graining Eq. (2) yields a Ginzburg-Landau free energy involving $\hat{C}_2^{II}$ and the two-point correlation of element $I = A$ or B, and $X_1(c)$ and $X_2(c)$ are interpolation functions (see text). The reciprocal lattice vector $\vec{k}_{10}^B$ is used to set the scale of the triangular lattice favored by element B in this work, while $\vec{k}_{ij}^A$ denotes the lattice vectors in the $(i,j) = (1,0)$ or $(i,j) = (1,1)$ directions, which are used to define a square crystal symmetry for element A. For simplicity, gradients in the average density n_o are neglected in this term. Variations of n_o through the interface are controlled through variations in the amplitudes and concentration. The resulting free coarse-grained energy is given by:

$$\begin{aligned}
F_{\mathrm{CG}} = \int d\vec{r}\Big\{ & \frac{1}{2}n_0^2 - \frac{\eta}{6}n_0^3 + \frac{\chi}{12}n_0^4 + \omega(n_0+1)\Delta F_{\mathrm{mix}}(c) + \alpha|\nabla c|^2 + \left(1 - \eta n_0 + \chi n_0^2\right)\left(\mathcal{A}_1^2 + \mathcal{A}_2^2 + \mathcal{B}_1^2 + \mathcal{B}_2^2\right.\\
& \left. + \mathcal{C}_1^2 + \mathcal{C}_2^2 + \mathcal{C}_3^2\right) + \left(4\chi n_0 - 2\eta\right)\left(\mathcal{A}_1\mathcal{A}_2\mathcal{B}_1 + \mathcal{A}_1\mathcal{A}_2\mathcal{B}_2 + \mathcal{C}_1\mathcal{C}_2\mathcal{C}_3\right) + \frac{\chi}{2}\left(\mathcal{A}_1^4 + \mathcal{A}_2^4 + \mathcal{B}_1^4 + \mathcal{B}_2^4 + \mathcal{C}_1^4 + \mathcal{C}_2^4 + \mathcal{C}_3^4\right)\\
& + 2\chi\mathcal{A}_1^2\mathcal{B}_1\mathcal{B}_2 + 2\chi\mathcal{A}_2^2\mathcal{B}_1\mathcal{B}_2 + 2\chi\mathcal{A}_1^2\left(\mathcal{A}_2^2 + \mathcal{B}_1^2 + \mathcal{B}_2^2 + \mathcal{C}_1^2 + \mathcal{C}_2^2 + \mathcal{C}_3^2\right) + 2\chi\mathcal{A}_2^2\left(\mathcal{B}_1^2 + \mathcal{B}_2^2 + \mathcal{C}_1^2 + \mathcal{C}_2^2 + \mathcal{C}_3^2\right)\\
& + 2\chi\mathcal{B}_1^2\left(\mathcal{B}_2^2 + \mathcal{C}_1^2 + \mathcal{C}_2^2 + \mathcal{C}_3^2\right) + 2\chi\mathcal{B}_2^2\left(\mathcal{C}_1^2 + \mathcal{C}_2^2 + \mathcal{C}_3^2\right) + 2\chi\mathcal{C}_1^2\mathcal{C}_2^2 + 2\chi\mathcal{C}_1^2\mathcal{C}_3^2 + 2\chi\mathcal{C}_2^2\mathcal{C}_3^2 - 2\left(X_1(c)\hat{C}_2^{AA}\left(|\vec{k}_{10}^A|\right)\right.\\
& \left. + X_2(c)\hat{C}_2^{BB}\left(|\vec{k}_{10}^A|\right)\right)\left(\mathcal{A}_1^2 + \mathcal{A}_2^2\right) - 2\left(X_1(c)\hat{C}_2^{AA}\left(|\vec{k}_{11}^A|\right) + X_2(c)\hat{C}_2^{BB}\left(|\vec{k}_{11}^A|\right)\right)\left(\mathcal{B}_1^2 + \mathcal{B}_2^2\right) - 2\left(X_1(c)\hat{C}_2^{AA}\left(|\vec{k}_{10}^B|\right)\right.\\
& \left. + X_2(c)\hat{C}_2^{BB}\left(|\vec{k}_{10}^B|\right)\right)\left(\mathcal{C}_1^2 + \mathcal{C}_2^2 + \mathcal{C}_3^2\right) - \frac{1}{|\vec{k}_{10}^A|^2}\left(X_1(c)\hat{C}''^{AA}_2\left(|\vec{k}_{10}^A|\right) + X_2(c)\hat{C}''^{BB}_2\left(|\vec{k}_{10}^A|\right)\right)\left[\left|\left(i\vec{k}_{10}^A\cdot\nabla\right)\mathcal{A}_1\right|^2\right.\\
& \left. + \left|\left(i\vec{k}_{10}^A\cdot\nabla\right)\mathcal{A}_2\right|^2\right] - \frac{1}{|\vec{k}_{11}^A|^2}\left(X_1(c)\hat{C}''^{AA}_2\left(|\vec{k}_{11}^A|\right) + X_2(c)\hat{C}''^{BB}_2\left(|\vec{k}_{11}^A|\right)\right)\left[\left|\left(i\vec{k}_{11}^A\cdot\nabla\right)\mathcal{B}_1\right|^2 + \left|\left(i\vec{k}_{11}^A\cdot\nabla\right)\mathcal{B}_2\right|^2\right]\\
& - \frac{1}{|\vec{k}_{10}^B|^2}\left(X_1(c)\hat{C}''^{AA}_2\left(|\vec{k}_{10}^B|\right) + X_2(c)\hat{C}''^{BB}_2\left(|\vec{k}_{10}^B|\right)\right)\left[\left|\left(i\vec{k}_{10}^B\cdot\nabla\right)\mathcal{C}_1\right|^2 + \left|\left(i\vec{k}_{10}^B\cdot\nabla\right)\mathcal{C}_2\right|^2 + \left|\left(i\vec{k}_{10}^B\cdot\nabla\right)\mathcal{C}_3\right|^2\right]\Big\},
\end{aligned} \tag{A1}$$

where $\Delta F_{\mathrm{mix}}(c)$ is defined in Eq. (3).

[1] A. Karma and W.-J. Rappel, Phys. Rev. E **53**, R3017 (1996).

[2] J. Friedli, J. L. Fife, P. Di Napoli, and M. Rappaz, Metall. Mater. Trans. A **44**, 5522 (2013).

[3] T. Haxhimali, A. Karma, F. Gonzales, and M. Rappaz, Nat. Mater. **5**, 660 (2006).

[4] S. Henry, T. Minghetti, and M. Rappaz, Acta Mater. **46**, 6431 (1998).

[5] F. Gonzales and M. Rappaz, Metall. Mater. Trans. A **37**, 2797 (2006).

[6] L. V. Mikheev and A. A. Chernov, J. Cryst. Growth **112**, 591 (1991).

[7] A. A. Chernov, J. Cryst. Growth **264**, 499 (2004).

[8] K.-A. Wu and A. Karma, Phys. Rev. B **76**, 184107 (2007).

[9] K.-A. Wu, C.-H. Wang, J. J. Hoyt, and A. Karma, Phys. Rev. B **91**, 014107 (2015).

[10] N. Provatas and K. Elder, *Phase-Field Methods in Material Science and Engineering* (Wiley, New York, 2010).

[11] B. Echebarria, R. Folch, A. Karma, and M. Plapp, Phys. Rev. E **70**, 061604 (2004).

[12] M. Plapp, Phys. Rev. E **84**, 031601 (2011).

[13] K. R. Elder and M. Grant, Phys. Rev. E **70**, 051605 (2004).

[14] J. Berry, K. R. Elder, and M. Grant, Phys. Rev. B **77**, 224114 (2008).

[15] J. Mellenthin, A. Karma, and M. Plapp, Phys. Rev. B **78**, 184110 (2008).
[16] V. Fallah, A. Korinek, N. Ofori-Opoku, N. Provatas, and S. Esmaeili, Acta Mater. **61**, 6372 (2013).
[17] N. Provatas and S. Majaniemi, Phys. Rev. E **82**, 041601 (2010).
[18] G. I. Tóth, G. Tegze, T. Pusztai, G. Tóth, and L. Gránásy, J. Phys.: Condens. Matter **22**, 364101 (2010).
[19] G. I. Tóth and N. Provatas, Phys. Rev. B **90**, 104101 (2014).
[20] N. Ofori-Opoku, V. Fallah, M. Greenwood, S. Esmaeili, and N. Provatas, Phys. Rev. B **87**, 134105 (2013).
[21] N. Ofori-Opoku, Modelling microstructure evolution in materials science, Ph.D. thesis, McMaster University, Department of Materials Science and Engineering, 2013.
[22] K.-A. Wu, A. Adland, and A. Karma, Phys. Rev. E **81**, 061601 (2010).
[23] S. Majaniemi and N. Provatas, Phys. Rev. E **79**, 011607 (2009).
[24] M. Greenwood, N. Ofori-Opoku, J. Rottler, and N. Provatas, Phys. Rev. B **84**, 064104 (2011).
[25] N. Ofori-Opoku, J. Stolle, Z.-F. Huang, and N. Provatas, Phys. Rev. B **88**, 104106 (2013).
[26] K. R. Elder, N. Provatas, J. Berry, P. Stefanovic, and M. Grant, Phys. Rev. B **75**, 064107 (2007).
[27] M. Greenwood, N. Provatas, and J. Rottler, Phys. Rev. Lett. **105**, 045702 (2010).
[28] M. Greenwood, J. Rottler, and N. Provatas, Phys. Rev. E **83**, 031601 (2011).
[29] B. A. Jugdutt, Calculating the role of composition in the anisotropy of the solid-liquid interface via phase field crystal theory, Master's thesis, McGill University, Department of Physics, 2015.